

Solar flare accelerates nearly all electrons in a large coronal volume

Gregory D. Fleishman^{1,*}, Gelu M. Nita¹, Bin Chen¹, Sijie Yu¹, and Dale E. Gary¹

¹Center for Solar-Terrestrial Research, New Jersey Institute of Technology, Newark, NJ 07102, USA

ABSTRACT

Solar flares, driven by prompt release of free magnetic energy in the solar corona^{1,2}, are known to accelerate a substantial portion (10% or more)^{3,4} of available electrons to high energies. Hard X-rays, produced by high-energy electrons accelerated in the flare,⁵ require a high ambient density for their detection. This restricts the observed volume to denser regions that do not necessarily sample the entire volume of accelerated electrons.⁶ Here we report evolving spatially resolved distributions of thermal and nonthermal electrons in a solar flare derived from microwave observations that unveil the true extent of the acceleration region. These distributions reveal a volume filled with only (or almost only) nonthermal electrons, while being depleted of the thermal plasma, indicating that all electrons have experienced a prominent acceleration there. This volume is isolated from a surrounding, more typical flare plasma of mainly thermal particles with a smaller proportion of nonthermal electrons. This highly efficient acceleration happens in the same volume where the free magnetic energy is being released²; thus, it demonstrates a high conversion efficiency of magnetic energy directly into the acceleration of charged particles.

1 The microwave analysis is performed using imaging spectroscopy data from the Expanded Owens
2 Valley Solar Array (EOVSA) described in detail elsewhere². We employ independent pixel-to-pixel and
3 time-to-time spectral model fitting of these microwave imaging spectroscopy data to obtain evolving,
4 spatially resolved distributions (maps) of suprathermal and thermal electrons. These maps pinpoint
5 the location and shape of the evolving acceleration region in a large solar flare that occurred on 2017
6 September 10 (Fig. 1). This now famous flare has attracted extraordinary attention as it demonstrates
7 several “textbook” flare properties, which were observed with unprecedented coverage and resolution
8 across the electromagnetic spectrum^{7–14}.

9 Fig. 2 displays an example of these parameter maps for one time frame; the entire evolution is
10 illustrated in Supplementary Video S1. Fig. 2 also shows two regions of interest (ROIs), ROI1 and ROI2,
11 kept fixed for all analyzed time frames, which inscribe two areas having the most reliable spatially-resolved
12 spectra and, thus, the most reliable model spectral fitting diagnostics (See Methods). ROI1 inscribes the
13 area where the fast and strong release of coronal magnetic energy has been measured², while ROI2 is a
14 reference area of more typical flare plasma, outside the acceleration region, to be used for comparison.

15 We focus on ROI1, where the fast, strong release of magnetic energy occurred during the main flare
16 phase², thus pinpointing the very energy release region. Fig. 2d shows that ROI1 inscribes an extended
17 area (corresponding to an estimated volume of $\sim 1.67 \times 10^{27}$ cm³; see Methods), in which the number
18 density of suprathermal electrons with high energies above 20 keV is very large—up to $\sim 10^{10}$ cm⁻³. In
19 contrast, the number density of thermal electrons in ROI1, shown in Fig. 2c, is undetectably small (see

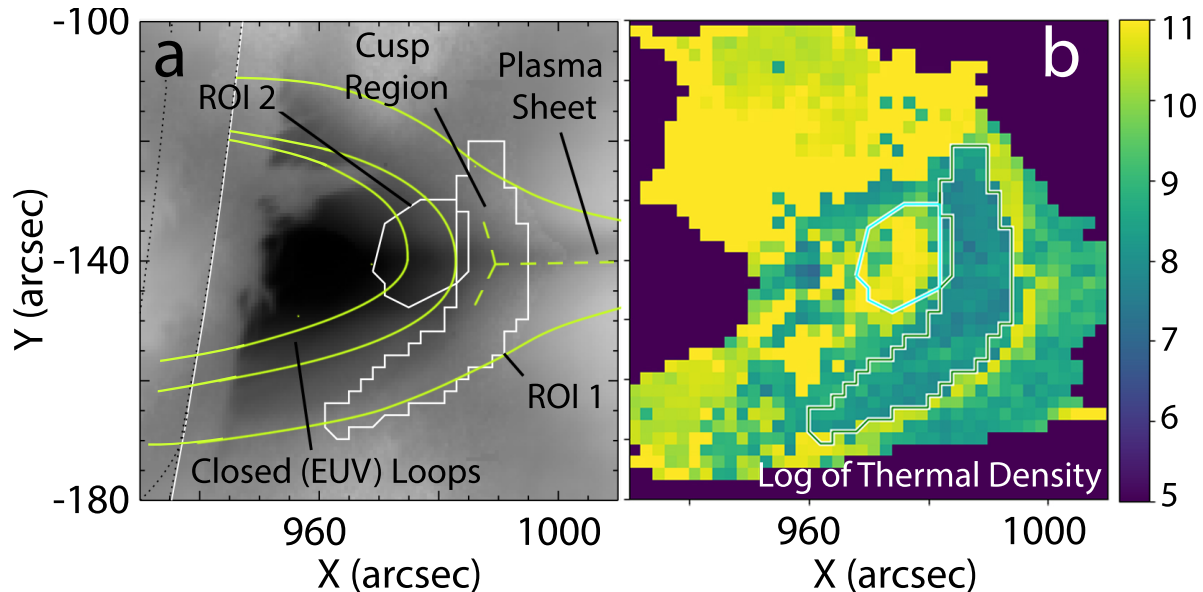


Figure 1. Thermal plasma in the context of magnetic morphology in the 2017-Sep-10 solar flare. (a) The plot shows EUV brightness distribution (image) in the context of the hand-drawn magnetic field lines outlining closed, post-reconnection loops, cusp region including a so-called Y-point, and the vertical plasma sheet. ROI1 and ROI2 employed in the analysis are also shown. (b) Distribution of the median values of the thermal plasma density, log scale, obtained from the microwave data using MCMC simulations; see Methods. Strong depletion of the thermal number density is apparent inside ROI1.

20 Methods): the map contains an extended thermal density “hole” roughly coinciding with ROI1. This
 21 directly implies that the number density of suprathermal electrons is much larger than that of the thermal
 22 electrons in the region where the release of magnetic energy takes place.

23 Supplementary Video S1 demonstrates that the gap in the thermal electron distribution holds for the
 24 entire duration of the analyzed four-minute episode around the peak of the flare, although its shape evolves
 25 and shows an overall outward motion (to the right in the figure), and it continues to match the region of
 26 enhanced suprathermal electron density. These spatiotemporal evolutions show that, during the entire
 27 episode, ROI1 and ROI2 differ fundamentally in character: suprathermal electrons dominate in ROI1,
 28 while the thermal electrons dominate in ROI2. The suprathermal electrons in ROI1 appear to have been
 29 accelerated in place, rather than transported there from elsewhere (See Methods).

30 Therefore, ROI1 combines three properties: (i) fast release of a large amount of magnetic energy²;
 31 (ii) depletion of thermal plasma; and (iii) presence of a dense population of suprathermal electrons,
 32 presumably accelerated due to the magnetic energy release. This combination of properties implies that
 33 we have resolved the heart of the solar flare—the very acceleration region, which places strong constraints
 34 on the physical mechanism that drives the acceleration of electrons in the flare. Indeed, any mechanism
 35 capable of producing a suprathermal particle population has to extract a fraction of charged particles from
 36 the thermal plasma pool and increase individual energies of those particles greatly. As a result, at this
 37 acceleration stage the number of accelerated suprathermal particles increases at the expense of the thermal
 38 particles, whose number density proportionally decreases. In our case, ROI1 has a lower (possibly much

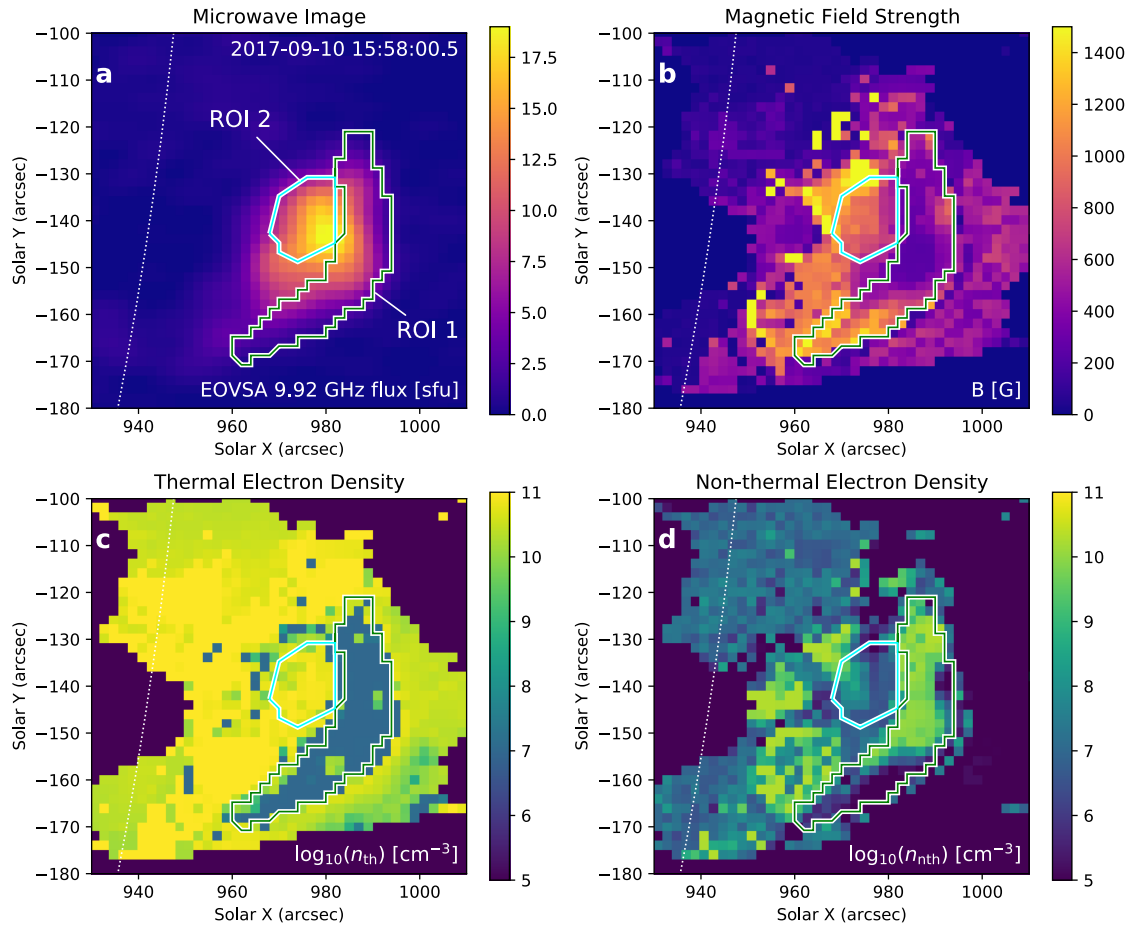


Figure 2. Spatial Distributions of Flare Parameters. a: EOVSA map at 9.92 GHz taken at 15:58 UT. b–d: Maps of the magnetic field (b), thermal plasma density (c), and nonthermal plasma density (d) derived for the same time from the bulk model spectral fitting (see Methods). ROI1 inscribes the hole in the distribution of thermal plasma, which also corresponds to a peak in the number density of the suprathermal electrons. ROI2 inscribes a reference area; see Methods. The dotted arc shows the solar limb. Note that due to different processing panel (c) differs slightly from Fig. 1b, which was produced by the more thorough but time-consuming MCMC method; see Methods.

39 lower) than 10% proportion of thermal plasma in a region of high suprathermal electron density (See
 40 Methods). This means that a large fraction, essentially all, of the thermal electrons originally present in
 41 this volume have been converted to the suprathermal electron population during (and, presumably, due to)
 42 this energy release. We conclude that the magnetic energy release in the solar flare offers a highly efficient
 43 engine for particle acceleration, which is capable of converting essentially all ambient electrons with
 44 thermal energies (e.g., less than ≈ 1 keV) into a suprathermal population of electrons with high energies
 45 exceeding 20 keV (See Methods).

46 The release of free magnetic energy, quantified by the fast decay of the magnetic field at the rate

47 $\dot{B} \approx 5 \text{ G s}^{-1}$, has been suggested to be driven by turbulent magnetic reconnection within an extended
 48 volume of the cusp region of the flare². This is motivated by the inferred highly enhanced turbulent
 49 magnetic diffusivity, $\nu \sim 10^{15} \text{ cm}^2 \text{ s}^{-1}$, and the associated strong electric field, $E \sim 20 \text{ V cm}^{-1}$, in that
 50 extended volume².

51 The fundamental force capable of producing work on charged particles is the electric force. The
 52 acceleration efficiency is specified by a balance between the energy gain due to the electric field and
 53 energy loss through collisions, which defines a critical value of the electric field, called the Dreicer field,
 54 E_D ¹⁵. The condition for run-away acceleration is $E \gg E_D$, which is called a “super-Dreicer” electric field.
 55 The electric field inferred from the magnetic field decay², $\sim 20 \text{ V cm}^{-1}$ is many orders of magnitude
 56 larger than the estimated Dreicer field, which is $E_D \sim 10^{-4} \text{ V cm}^{-1}$.

57 To support the simultaneous acceleration of literally all ambient electrons in a macroscopic volume
 58 such as ROI1, this strong super-Dreicer field must be present over a substantial portion of ROI1. As noted
 59 above, this is consistent with the observed simultaneous decay of the magnetic field over the entire ROI1²,
 60 indicative of turbulent magnetic reconnection, where the dissipation of the magnetic energy takes place
 61 throughout the volume. This is in contrast to the alternative view that all acceleration takes place in one or
 62 a few isolated points (X- or O-points¹⁶) favorable for macroscopic reconnection.

63 From this work there emerges a consistent picture of particle acceleration in the magnetic energy
 64 release region: (i) the decay of the magnetic field due to turbulent magnetic reconnection produces strong
 65 super-Dreicer electric field over an extended volume; (ii) this strong electric field does work over literally
 66 all ambient particles, which boosts their energies up to 20 keV and higher; (iii) this acceleration process is
 67 so efficient and persistent that it does not leave any measurable thermal plasma component compared with
 68 the highly dominant suprathermal component.

69 Models of particle acceleration due to magnetic reconnection including 2D and 3D particle-in-cell
 70 (PIC) simulations, as well as a novel large-scale kinetic simulation approach *kglobal*^{17,18}, suggest that
 71 efficiency of the acceleration is linked to a ratio of the reconnecting (dissipating) component B_{rec} of the
 72 total magnetic field and the remaining component, called the guide field B_g ¹⁹, does not explicitly take
 73 part in the reconnection. According to the models^{17,18,20–22}, efficient acceleration requires that B_{rec} is
 74 larger than B_g . We check this expectation with our data. Although we cannot properly separate these
 75 two components observationally, we can compare the observed total magnetic field, $B_{tot}(t)$, at a given
 76 time and location with its value B_{steady} near the end of the decay period, when it becomes steady²³. We
 77 estimate B_{steady} at each location within ROI1 as the mean B evaluated over the last 20 s of the four-minute
 78 episode². B_{steady} serves as an estimate for the magnetic field component that does not participate in the
 79 energy release process, which includes B_g . Then, for each pixel, we form a ratio $r_B(t) = B_{tot}(t)/B_{steady}$,
 80 where $B_{tot}(t)$ is the instantaneous value of the magnetic field inferred from the spectral model fit, which
 81 includes both decaying and steady components of the magnetic field. If the observed $r_B \gg 1$, then it is
 82 likely that $B_{rec}/B_g \gg 1$ too (small guide field case); thus, $r_B \gg 1$ could be viewed as a good proxy for
 83 efficient acceleration. We focus on the first two minutes of our four-minute episode, where the condition
 84 $r_B \gg 1$ holds for many pixels and times.

85 We investigate the relationship between parameters n_{nth} and δ of the suprathermal electron component
 86 derived from the spectral fit and the ratio r_B , where the nonthermal number density exceeds the thermal
 87 one. We did not find any correlation of the number density of the suprathermal electrons with r_B . This is
 88 consistent with the observed strong efficiency of the acceleration, which results in virtually all ambient
 89 electrons being accelerated. What is correlated with acceleration efficiency is the powerlaw spectral index
 90 δ , as shown in Fig. 3. The correlation is such that a larger r_B (proxy for small guide field case) implies a

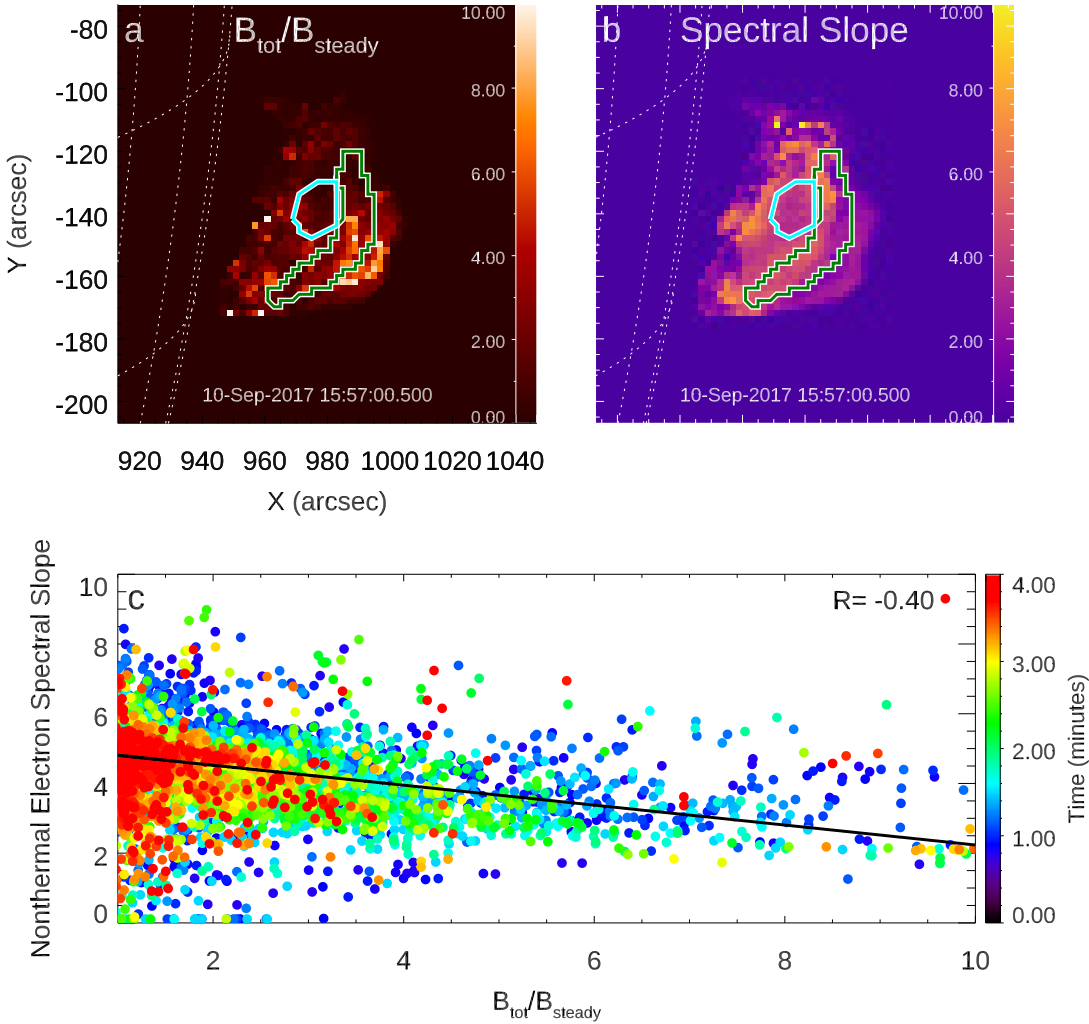


Figure 3. Spectral slope of the suprathermal component vs reconnecting magnetic field. The upper row panels display the maps of (a) the inferred $r_B = B_{\text{tot}}/B_{\text{steady}}$ ratio and (b) the suprathermal electron energy spectral slope, averaged over the first 5 time frames (20 seconds) of the full four-minute interval. The ROI1 and ROI2 regions are marked, respectively, by green and cyan contours in both panels. (c) Dot symbols show the spectral index δ obtained from the ROI1 model fit for each pixel and time vs the running value of the r_B ratio. The correlation data are plotted for the analyzed four-minute interval, color coded as time increases, as shown by the right side color bar. The solid line shows the linear fit to the data over the first two minutes, when most of the energy release takes place, which corresponds to a correlation coefficient $R = -0.40$. An animated version of this figure (Supplementary Video S2) showing all time frames used in this analysis is provided as supplemental material.

91 smaller spectral index (harder energy spectrum) thus validating the theoretical expectations¹⁸. A simplistic
 92 interpretation of this relationship is that having more free magnetic energy (larger r_B) permits acceleration
 93 to higher energies, thus, producing a flatter distribution of the accelerated electrons over energy.

94 In addition, our observations reveal that the suprathermal electrons, generated in a region where
95 virtually all ambient electrons are accelerated, remain almost perfectly isolated from the surrounding
96 cooler plasma for a time period much longer than the source transit time, even though the system does not
97 contain any “solid walls” that would hold suprathermal particles in. This means that the system contains
98 a highly efficient physical process or magnetic topology that traps the suprathermal particles within the
99 volume they occupy. Otherwise, the suprathermal particles would become much more uniformly mixed
100 with the ambient thermal particles, which is not observed. An important process capable of providing
101 this trapping is enhanced angular diffusion that reduces the particle mean free path²⁴. Such diffusion is
102 due to particle scattering by the turbulent magnetic field, which is also responsible for acceleration of the
103 particles. Although the need for this enhanced diffusion is strongly suggested by the observations, the
104 important characteristics of the corresponding turbulent magnetic field, such as their spectral and spatial
105 structure and evolution, remain unknown and call for dedicated modeling.

106 References

- 107 **1.** Yokoyama, T. & Shibata, K. Magnetic reconnection as the origin of X-ray jets and H α surges on the
108 Sun. *Nature* **375**, 42–44 (1995).
- 109 **2.** Fleishman, G. D. *et al.* Decay of the coronal magnetic field can release sufficient energy to power a
110 solar flare. *Science* **367**, 278–280 (2020).
- 111 **3.** Krucker, S. *et al.* Measurements of the Coronal Acceleration Region of a Solar Flare. *Astrophys. J.*
112 **714**, 1108–1119 (2010).
- 113 **4.** Krucker, S. & Battaglia, M. Particle Densities within the Acceleration Region of a Solar Flare.
114 *Astrophys. J.* **780**, 107 (2014).
- 115 **5.** Kontar, E. P. *et al.* Deducing Electron Properties from Hard X-ray Observations. *Space Science*
116 *Reviews* **159**, 301–355 (2011).
- 117 **6.** Holman, G. D. *et al.* Implications of X-ray Observations for Electron Acceleration and Propagation
118 in Solar Flares. *Space Science Reviews* **159**, 107–166 (2011).
- 119 **7.** Warren, H. P. *et al.* Spectroscopic Observations of Current Sheet Formation and Evolution. *Astrophys.*
120 *J.* **854**, 122 (2018).
- 121 **8.** Gary, D. E. *et al.* Microwave and hard x-ray observations of the 2017 september 10 solar limb flare.
122 *The Astrophysical Journal* **863**, 83 (2018).
- 123 **9.** Longcope, D., Unverferth, J., Klein, C., McCarthy, M. & Priest, E. Evidence for Downflows in
124 the Narrow Plasma Sheet of 2017 September 10 and Their Significance for Flare Reconnection.
125 *Astrophys. J.* **868**, 148 (2018).
- 126 **10.** Hayes, L. A. *et al.* Persistent Quasi-periodic Pulsations during a Large X-class Solar Flare. *Astrophys.*
127 *J.* **875**, 33 (2019).
- 128 **11.** Chen, B. *et al.* Measurement of magnetic field and relativistic electrons along a solar flare current
129 sheet. *Nature Astronomy* **4**, 1140–1147 (2020).
- 130 **12.** Yu, S. *et al.* Magnetic Reconnection during the Post-impulsive Phase of a Long-duration Solar Flare:
131 Bidirectional Outflows as a Cause of Microwave and X-Ray Bursts. *Astrophys. J.* **900**, 17 (2020).

- 132 **13.** French, R. J., Matthews, S. A., van Driel-Gesztelyi, L., Long, D. M. & Judge, P. G. Dynamics of
133 Late-stage Reconnection in the 2017 September 10 Solar Flare. *Astrophys. J.* **900**, 192 (2020).
- 134 **14.** Reeves, K. K. *et al.* Hot Plasma Flows and Oscillations in the Loop-top Region During the 2017
135 September 10 X8.2 Solar Flare. *Astrophys. J.* **905**, 165 (2020).
- 136 **15.** Dreicer, H. Electron and ion runaway in a fully ionized gas. i. *Phys. Rev.* **115**, 238–249 (1959).
- 137 **16.** Priest, E. R. & Forbes, T. G. The magnetic nature of solar flares. *Astronomy and Astrophysics Review*
138 **10**, 313–377 (2002).
- 139 **17.** Drake, J. F., Arnold, H., Swisdak, M. & Dahlin, J. T. A computational model for exploring particle
140 acceleration during reconnection in macroscale systems. *Physics of Plasmas* **26**, 012901 (2019).
- 141 **18.** Arnold, H. *et al.* Electron acceleration during macroscale magnetic reconnection. *Phys. Rev. Lett.*
142 **126**, 135101 (2021).
- 143 **19.** Drake, J. F., Swisdak, M. & Fermo, R. The Power-law Spectra of Energetic Particles during Multi-
144 island Magnetic Reconnection. *ApJ* **763**, L5 (2013).
- 145 **20.** Dahlin, J. T., Drake, J. F. & Swisdak, M. The mechanisms of electron heating and acceleration during
146 magnetic reconnection. *Physics of Plasmas* **21**, 092304 (2014).
- 147 **21.** Dahlin, J. T., Drake, J. F. & Swisdak, M. Electron acceleration in three-dimensional magnetic
148 reconnection with a guide field. *Physics of Plasmas* **22**, 100704 (2015).
- 149 **22.** Dahlin, J. T. Prospectus on electron acceleration via magnetic reconnection. *Physics of Plasmas* **27**,
150 100601 (2020).
- 151 **23.** Kuridze, D. *et al.* Mapping the Magnetic Field of Flare Coronal Loops. *Astrophys. J.* **874**, 126
152 (2019).
- 153 **24.** Fleishman, G. D. & Toptygin, I. N. 712 p [FT13], vol. 388 of *Cosmic Electrodynamics. Astrophysics*
154 *and Space Science Library; Springer NY* (2013).

155 **Figure Legends**

156 **Figure 1. Thermal plasma in the context of magnetic morphology in the 2017-Sep-10 solar flare.**
157 (a) The plot shows EUV brightness distribution (image) in the context of the hand-drawn magnetic
158 field lines outlining closed, post-reconnection loops, cusp region including a so-called Y-point, and the
159 vertical plasma sheet. ROI1 and ROI2 employed in the analysis are also shown. (b) Distribution of the
160 median values of the thermal plasma density, log scale, obtained from the microwave data using MCMC
161 simulations; see Methods. Strong depletion of the thermal number density is apparent inside ROI1.

162 **Figure 2. Spatial Distributions of Flare Parameters.** a: EOVS map at 9.92 GHz taken at 15:58 UT.
163 b–d: Maps of the magnetic field (b), thermal plasma density (c), and nonthermal plasma density (d)
164 derived for the same time from the bulk model spectral fitting (see Methods). ROI1 inscribes the hole
165 in the distribution of thermal plasma, which also corresponds to a peak in the number density of the
166 suprathermal electrons. ROI2 inscribes a reference area; see Methods. The dotted arc shows the solar
167 limb. Note that due to different processing panel (c) differs slightly from Fig. 1b, which was produced by
168 the more thorough but time-consuming MCMC method; see Methods.

169 **Figure 3. Spectral slope of the suprathermal component vs reconnecting magnetic field.** The upper
 170 row panels display the maps of (a) the inferred $r_B = B_{\text{tot}}/B_{\text{steady}}$ ratio and (b) the suprathermal electron
 171 energy spectral slope, averaged over the first 5 time frames (20 seconds) of the full four-minute interval.
 172 The ROI1 and ROI2 regions are marked, respectively, by green and cyan contours in both panels. (c)
 173 Dot symbols show the spectral index δ obtained from the ROI1 model fit for each pixel and time vs the
 174 running value of the r_B ratio. The correlation data are plotted for the analyzed four-minute interval, color
 175 coded as time increases, as shown by the right side color bar. The solid line shows the linear fit to the data
 176 over the first two minutes, when most of the energy release takes place, which corresponds to a correlation
 177 coefficient $R = -0.40$. An animated version of this figure (Supplementary Video S2) showing all time
 178 frames used in this analysis is provided as supplemental material.

179 **Methods**

180 **Overview**

181 In this study we used the data set from the Expanded Owens Valley Solar Array²⁵ (EOVSA) described
 182 in an earlier paper². The model spectral fitting, its parameters and their uncertainties were described
 183 in the Supplementary Materials to that paper. The parameters used to create the evolving maps of the
 184 thermal and suprathermal electrons in the flare region are from the same spectral fits as those used for the
 185 magnetic field maps reported there. Here, we employed these maps of electron parameters to investigate
 186 the spatially resolved structure and evolution of the electron acceleration in the spatial area that showed
 187 the most prominent decay of the coronal magnetic field².

188 **Spatially Resolved Microwave Spectra and Selection of Regions of Interest**

189 Fig. S1 displays a representative set of the observed spatially resolved microwave spectra from pixels with
 190 an area of $2'' \times 2'' (\sim 2.1 \times 10^{16} \text{ cm}^2)$ and associated model spectral fits distributed over the flare region.
 191 For reference, the central panel shows a single microwave image¹ at 9.92 GHz taken at 15:58 UT, which
 192 corresponds to the main peak of the flare. The spectral fitting employs the model of the gyrosynchrotron
 193 source function with the account of the free-free component². We performed this model spectral fitting
 194 over all 60 time frames and over all pixels in these 60 map cubes, assuming a source depth along the line of
 195 sight (LOS) of 5.8 Mm (this corresponds to $8''$ on disk, which is a scale of features (loops) seen in the flare
 196 images). The primary region of interest, ROI1, indicated by the green contour, includes 137 image pixels
 197 that, under the same LOS depth assumptions, correspond to an estimated volume of $\sim 1.7 \times 10^{27} \text{ cm}^3$.
 198 Consequently, the reference region of interest ROI2 shown by the cyan contour, which encloses 49 pixels,
 199 corresponds to an estimated volume of $\sim 6.0 \times 10^{26} \text{ cm}^3$. The numbered points are pixels whose spectra
 200 and fits are shown in the other eight panels of the plot.

201 ROI1 inscribes the area where the most prominent decay of the magnetic field has been detected, a
 202 small portion of which was analyzed in the earlier paper². Here we analyze the entire ROI1 as it shows
 203 a coherent depletion of the thermal plasma and a high density of suprathermal electrons. The spatially
 204 resolved spectra (for example, pixels P1 and P4) from an upper portion of ROI1 have high signal-to-noise
 205 ratio and their spectral peaks occur within the frequency range observed by EOVSA. As a result, the
 206 model spectral fitting diagnostics employing such spectra are the most robust (see the next Section).
 207 In the bottom portion of ROI1, the spectra have lower signal-to-noise ratio (see example in pixel P6),

¹The instrumental beam is $113''.7/f[\text{GHz}] \times 53''.0/f[\text{GHz}]$. A circular restoring beam of FWHM $87''.9/f[\text{GHz}]$ was used, which is about $9''$ for 9.92 GHz shown in the Figure.

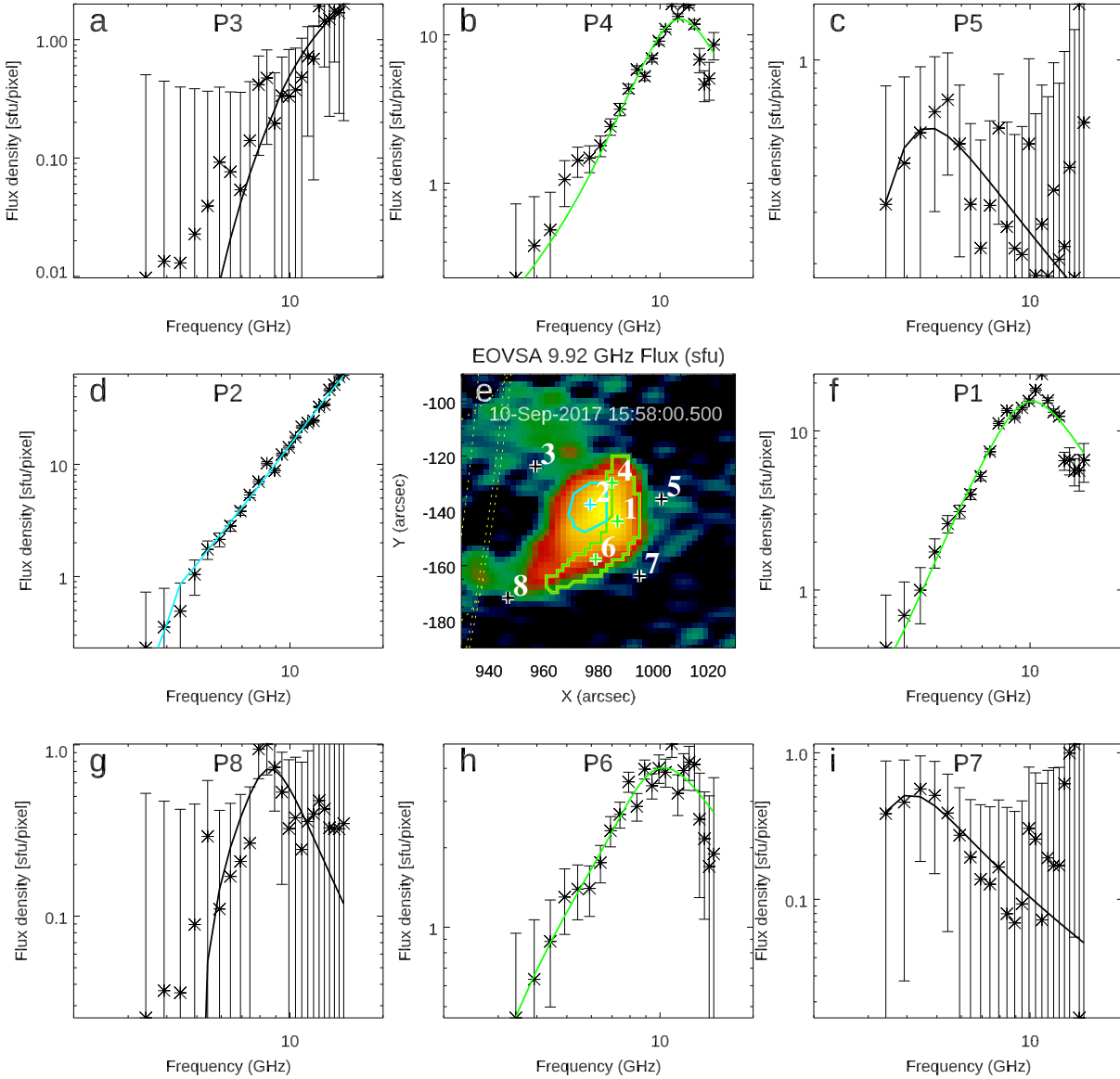


Fig. S1. Example spectra from various locations and associated model fits. The central panel shows a reference microwave image at 9.92 GHz at 15:58 UT. ROI1 and ROI2 are shown in green and blue, respectively. Plus signs, 1 to 8, indicate pixels, for which the observed spectra and model fits are shown in the remaining eight panels, each marked with P1 to P8. The asterisks with error bars show the data and the uncertainties at the 1-sigma level; the curves show the corresponding model spectral fits. The fluxes are given in Solar Flux Units (sfu): $1 \text{ sfu} = 10^4 \text{ Jy} = 10^{-22} \text{ W m}^{-2} \text{ Hz}^{-1} = 10^{-19} \text{ erg s}^{-1} \text{ cm}^{-2} \text{ Hz}^{-1}$.

208 especially at high frequencies, which can result in larger uncertainties of the spectral index that quantifies
 209 the suprathermal electron distribution over energy (see Supplemental Materials in the earlier paper²).

210 In the reference area ROI2, the signal-to-noise ratio is also high. The spectral peak is outside the

211 EOVSA frequency range indicative of high magnetic field in ROI2. The model spectral fitting of such
 212 spectra typically yields a reliable estimate of the thermal number density, while the magnetic field and
 213 suprathermal electrons are recovered with larger uncertainties (see the next Section).

214 Four other spectra from the figure corners show spectra from pixels P3, P5, P7, and P8. The signal-to-
 215 noise ratios are not great there; however, the fits are within the uncertainties and the spectra show expected
 216 trends: the spectral peak frequency is high from P3 and P8 locations close to the solar limb (which means
 217 high magnetic field strength), while the peak frequency is lower from higher locations P5 and P7 (which
 218 implies lower magnetic field strength). We note that because of high uncertainties of the data in the four
 219 “corner” cases, the uncertainties of the derived physical parameters are also large there. Although we
 220 present parameters from all these fits in Figure 2, we restrict our quantitative analysis to the most reliable
 221 spectra and fits from ROI1 and ROI2 and hence those four are excluded.

222 MCMC Validation of the Spectral Model Fit

223 The main reported result, that the number density of high-energy electrons is much larger within ROI1
 224 than that of the thermal plasma, is based on the model spectral fitting of the microwave data. Here we
 225 employ the Monte Carlo Markov Chain (MCMC) simulations, implemented by an open-source Python
 226 package *emcee*²⁶, to derive statistical distributions of the model fit parameters to quantify the confidence
 227 of this finding. This approach explores the full multi-dimensional space of the model fit parameters to
 228 both provide parameter distributions and reveal correlations between them. For this reason, it is much
 229 more time consuming than the speed-optimized GSFIT approach², with which the bulk model spectral
 230 fitting has been performed. We restrict our MCMC analysis to all pixels in a single time frame, the same
 231 as shown in Fig. 2, which takes considerably longer than the GSFIT analysis of the entire 60-frame time
 232 sequence, but a comparison of the MCMC result in Fig. 1b with the bulk fitting in Fig. 2c shows that the
 233 results are comparable and fully consistent.

234 Thermal and suprathermal electrons affect the microwave spectrum differently. The suprathermal
 235 electrons gyrating in the ambient magnetic field are responsible for *generation* of the microwave emission.
 236 In the optically thin regime (high frequencies) the contributions of each individual electron add up
 237 incoherently; thus, the microwave flux level of the emission is proportional to the number density of
 238 the suprathermal component. In the optically thick regime (low frequencies) the flux of the microwave
 239 emission is determined by the energy of the electron population responsible for the emission at a given
 240 frequency. For these reasons, the microwave diagnostics of the suprathermal electrons is robust provided
 241 that both low and high frequency spectral ranges are available.

The thermal electrons contribute much less to the radiation intensity. Their main effect on the
 microwave radiation spectrum is due to dispersion of electromagnetic waves; simplistically speaking, due
 to the index of refraction. In the plasma, the index of refraction depends on the plasma frequency ω_p ,
 which is defined by the number density of the ambient free electrons:

$$\omega_p^2 = \frac{4\pi e^2 n_{\text{tot}}}{m}, \quad (1)$$

where e and m are the charge and mass of the electrons, n_{tot} is the total number density of all ambient free
 electrons—both thermal n_{th} and suprathermal n_{nth} :

$$n_{\text{tot}} = n_{th} + n_{nth}. \quad (2)$$

242 As n_{th} , and thus n_{tot} , increases, the microwave flux decreases at low frequencies as illustrated in Supple-
243 mentary Video S3. Thus, the diagnostic of n_{th} is primarily based on the microwave spectral shape at low
244 frequencies. If $n_{th} \gg n_{nth}$, then $n_{tot} \approx n_{th}$ offering the diagnostics of the thermal electron number density.
245 The MCMC analysis of a spectrum (from a pixel inside ROI2) that yields a well-constrained thermal
246 number density is shown in Fig. S2. The Figure layout is as follows. The stand-alone upper-right
247 panel shows a measured spectrum from a pixel within ROI2 (open circles with error bars) and a set
248 of theoretical trial spectra (blue) consistent with the data. The panels placed over the diagonal show
249 statistical distributions (histograms) of the trial fits for all 6 model parameters. The remaining panels
250 show correlations between all possible pairs of these parameters. In this case the distribution of thermal
251 plasma number density is very narrow; thus, this parameter is well constrained (see, also, the next Section).
252 This is due to the well-measured low-frequency part of the spectrum, whose deviation from a simple
253 power-law permits this thermal density diagnostic as explained above. In contrast, other parameters
254 have broader statistical distributions and, thus, they are not that well constrained. This is due to the
255 absence of the optically thin part of the measured spectrum, because the spectral peak extends beyond
256 the EOVS frequency range. Though the distribution of the suprathermal electron number density is
257 broad, its relatively low most-probable value is consistent with the dominance of the thermal electrons,
258 $n_{th} > n_{nth}$.

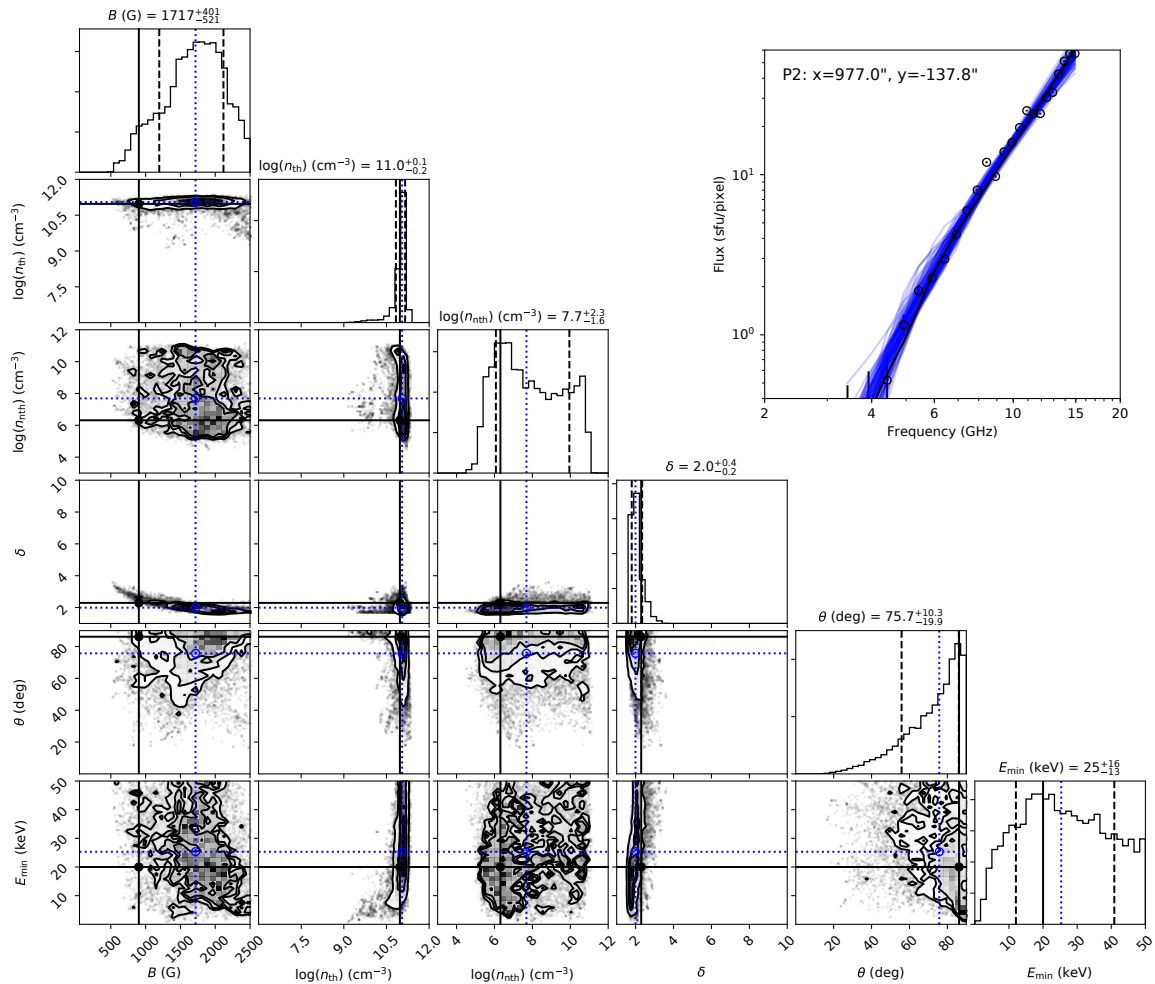


Fig. S2. MCMC probability distributions of the fit parameters for an example pixel in ROI2. The results are for pixel P2 located at $x = 977.0''$ and $y = -137.8''$ as marked in Fig. S1. Solid black horizontal/vertical lines in each panel indicate the best-fit values from the GSFIT minimization. Dotted blue horizontal/vertical lines mark the median values of the MCMC probability distributions. Dashed lines in the histograms along the diagonal indicate ± 1 -sigma standard deviation of a given parameter. Off-diagonal panels show correlations between all possible pairs of parameters shown as two-dimensional histograms of the probability distributions. The contour levels represent 39.3%, 60%, and 80% of the maximum. The outer contour level is selected to represent approximately the 1-sigma region of a 2D Gaussian distribution ($1 - e^{-0.5}$).

The case when $n_{th} \ll n_{nth}$ is more problematic for the thermal plasma diagnostics, because now $n_{tot} \approx n_{nth}$ and the thermal plasma density is defined by the difference

$$n_{th} = n_{tot} - n_{nth} \ll n_{tot}, \quad (3)$$

259 which is intrinsically less constrained given the uncertainties of the inputs. Thus, if the contribution of the

260 suprathermal electrons to the total ambient density dominates, it is problematic to obtain well-constrained
 261 values of the thermal number density separately. In such a situation we can only confidently conclude that
 262 $n_{th} \ll n_{nth}$, which would in fact confirm that most of the available ambient electrons have been accelerated
 263 to high energies. The results of the MCMC simulations for a pixel from ROI1 are shown in Fig. S3, which
 264 has the same layout as Fig. S2. Here, the spectrum contains the peak. The distributions of the magnetic
 265 field, suprathermal electron density, and their spectral index are narrow; thus, these parameters are well
 266 constrained. The suprathermal electron number density is high, of the order of $n_{nth} \sim 10^{10} \text{ cm}^{-3}$. In
 267 contrast, the distribution of the thermal plasma number density is broad. It favors low n_{th} values, while
 268 falling steeply for higher values. These distributions show that the thermal density contribution to the
 269 total ambient number density n_{tot} is undetectable compared with the nonthermal one, thus, confirming that
 270 $n_{th} \ll n_{nth}$: the median values of n_{th} are less than 5–10% of n_{nth} and even the upper limit values computed
 271 as $n_{th} + 1\sigma_{n_{th}}$ are less than $\sim 30\%$ of n_{nth} at many pixels within ROI1.

272 The maps of the thermal and suprathermal electron densities obtained from the MCMC simulations for
 273 the entire field of view are shown in Fig. S4. They agree within the uncertainties with those obtained using
 274 GSFIT in Fig. 2. This confirms the reliability of the results derived using the fast model spectral fitting
 275 method employed in GSFIT. One apparent disagreement between Fig. S4a and Fig. 2c is the thin line of
 276 enhanced thermal density just to the right from ROI1 in the MCMC case. Although, this feature is also
 277 present in Fig. 2c it is made less apparent because the density falls less steeply, extending the light yellow
 278 colors higher in altitude and reducing the contrast. The reason for this different appearance of the maps is
 279 that Fig. 2c displays the most likely parameter value from the GSFIT analysis, while Fig. S4a displays the
 280 median value from the corresponding statistical distribution of the parameter from the MCMC simulations
 281 (cf. Fig. S3 and Fig. S2). When the uncertainties of the derived parameters are small (their statistical
 282 distribution is narrow), then the GSFIT value is very close to the median MCMC value. However, in
 283 the area to the right of ROI1, uncertainties of the derived parameters are larger, resulting in the different
 284 appearance of these maps, even though the values are consistent with each other within uncertainties as
 285 has been said.

286 Panel c of Fig. S4 illustrates the dominance of the suprathermal component in ROI1 by showing
 287 $\log(n_{th,max}/n_{nth})$, where $n_{th,max}$ is represented as the median value of $n_{th} + 1\sigma_{n_{th}}$ of n_{th} in MCMC. A
 288 diverging colormap is selected for this plot, where white color means $\log(n_{th,max}/n_{nth}) = 0$. The blue/white
 289 region shows up as a distinctive feature of ROI1 with the ratio $\log(n_{th,max}/n_{nth})$ ranging from 10% to
 290 30%.

291 Note the nonthermal number density n_{nth} is sensitive to the value of the low-energy cutoff E_{min} ,
 292 which we adopted to be fixed at 20 keV in GSFIT. In our MCMC test we allow this parameter to vary.
 293 The assumption that $E_{min} = 20 \text{ keV}$ is proved valid in most regions of the map except in ROI1 (see the
 294 map of MCMC constrained E_{min} in Fig. S4d), where the median values of E_{min} reach 40 to 50 keV (see
 295 the sensitivity of the gyrosynchrotron spectrum to E_{min} in Supplementary Video S3). Although such a
 296 concentration of nonthermal electrons can be due either to acceleration in place or confinement of a
 297 transported electron population from elsewhere (e.g. the X point above)¹¹, the map of E_{min} shows that
 298 it is about two times larger in ROI1 than in the surroundings, which is rather difficult to account for
 299 without bulk electron acceleration in ROI1. The simultaneous decay of magnetic field in this same region
 300 is additional support for this. We thus conclude that the suprathermal electrons in ROI1 not only have a
 301 higher number density n_{nth} , but also are accelerated in bulk to a higher energy well separated from the
 302 thermal, Maxwellian component. In general, having larger E_{min} may imply smaller n_{nth} for the same
 303 spectral slope. However, the cross-correlation plots between the parameters shown in the bottom row of

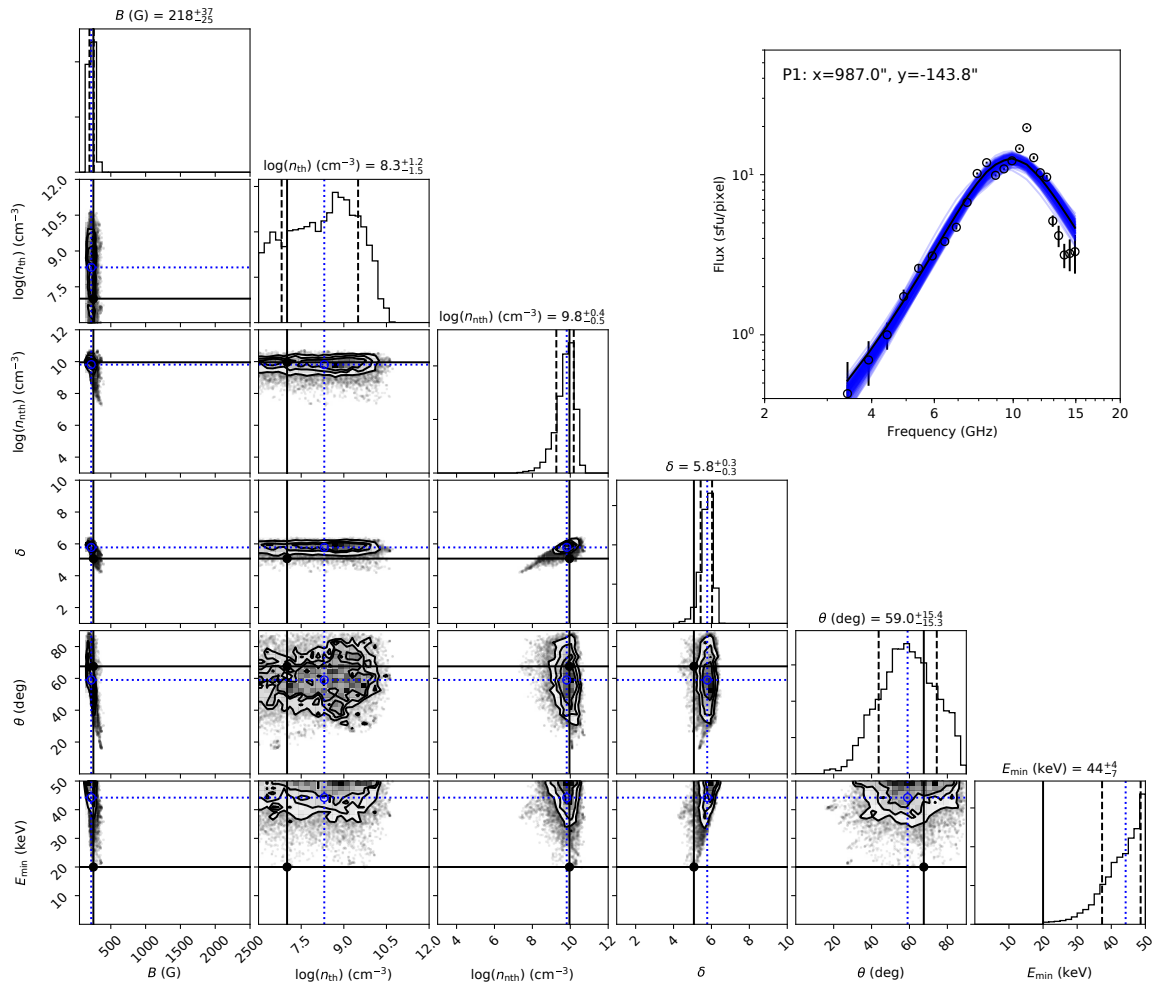


Fig. S3. MCMC probability distributions of the fit parameters for an example pixel in ROI1. The figure layout is identical to Fig. S2, but showing the parameters for pixel P1 located at $x = 987.0''$ and $y = -143.8''$ as marked in Fig. S1.

304 Fig. S2 demonstrate that E_{\min} correlates with δ in such a way that larger E_{\min} corresponds to larger δ
 305 (softer spectra). As a result of this correlation, n_{nth} does not correlate with E_{\min} ; thus, the conclusion of
 306 the high nonthermal number density is robust and does not depend strongly on the particular choice of
 307 E_{\min} .

308 **A consistency Check: Comparison of Microwave and Extreme Ultra Violet Diagnostics of** 309 **the Coronal Thermal Plasma**

310 A well-established way of probing thermal coronal plasma is using Extreme Ultra Violet (EUV) emission,
 311 which is a combination of line emission from ions, primarily iron, in various ionization states (and, thus,
 312 is temperature-sensitive) and a continuum due to bremsstrahlung. Here we employ EUV data taken by
 313 SDO/AIA in six narrow passbands sensitive to EUV emission from the corona. For each pixel within

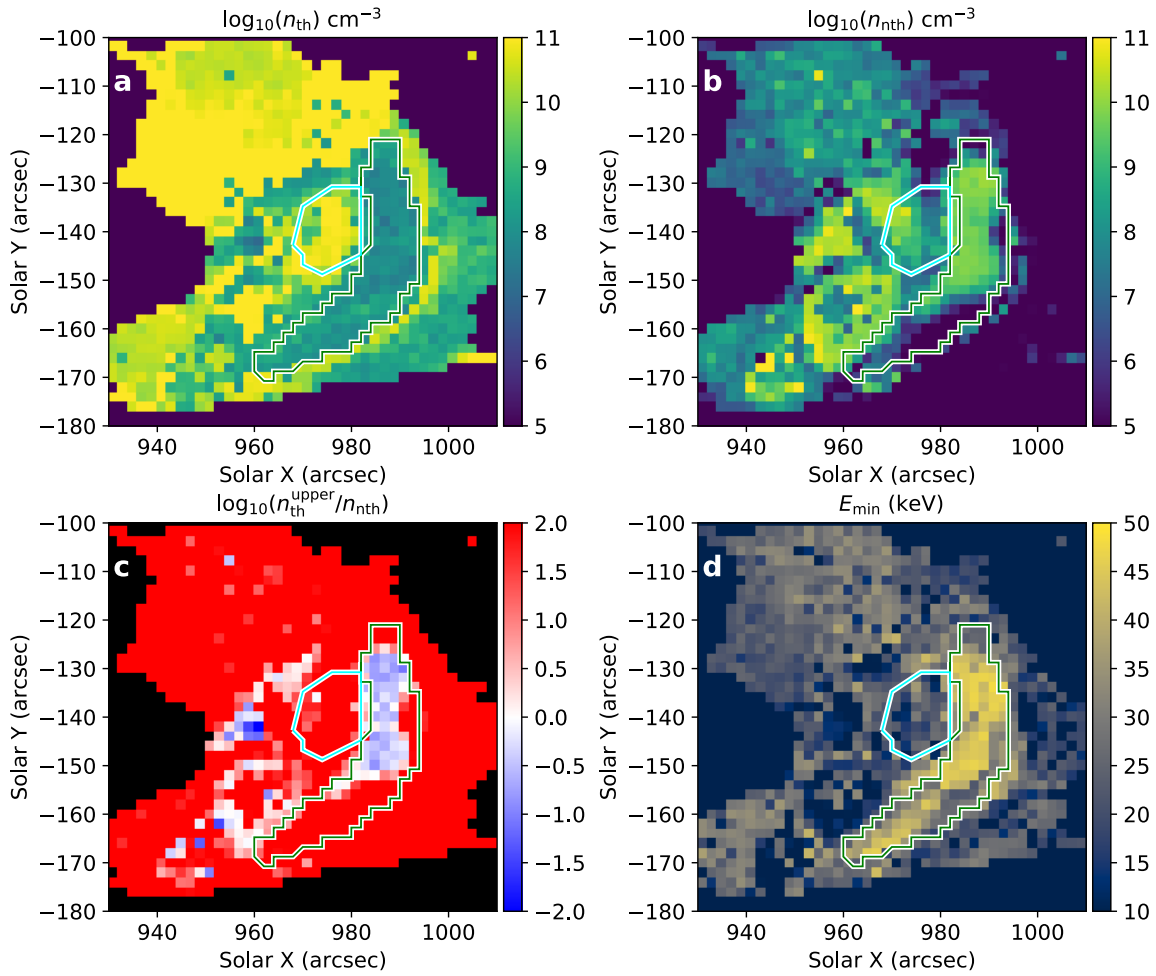


Fig. S4. MCMC constrained maps of the thermal and suprathermal electron parameters. a: Thermal electron number density n_{th} . For each pixel, the median value of the MCMC probability distribution is shown. b: Similar to a, but for the non-thermal electron number density n_{nth} . c: Map of the ratio of the upper limit of the thermal number density n_{th}^{upper} (defined as one σ above the median $n_{th} + \sigma_{n_{th}}$) to the nonthermal number density n_{nth} . d: Similar to a, but for the low-energy cutoff E_{min} .

314 the FOV we used to analyze the microwave emission, we applied a regularized differential emission
 315 measure (DEM) inversion²⁷ technique, from which we derived the Emission Measure ($EM = \int_{LOS} n_{th}^2 dL$,
 316 where dL is the differential column depth along the LOS) as a moment of the DEM. The thermal number
 317 density is then estimated as $n_{th} = \sqrt{EM/L}$, where L is 5.8 Mm, as adopted for the microwave spectral
 318 model fitting. The EM distribution is shown in Fig. S5a. Due to rather strong EUV emission, the EM map
 319 contains saturated areas and diffraction artifacts. Therefore, for quantitative analysis we selected a small
 320 rectangular area within ROI2 that avoids these artifacts to the extent possible.

321 Direct pixel-to-pixel comparison, even in case of a perfect co-alignment, would be inconclusive in our

322 case for the following reasons: (i) the pixel sizes of AIA and EOVSAs are different (0.6'' and 2'',
323 respectively); (ii) the time cadence of data used for the analysis are different (12 s and 4 s, respectively).
324 Therefore, we compare statistical distributions, rather than individual values, of the thermal electron
325 number density, obtained from these two different data sets.

326 We consider a single 12 s time range of the AIA data in a small rectangle area, marked in dark blue
327 in Fig S5, free from strong artifacts, which contains 100 AIA pixels, and three 4 s time ranges of the
328 EOVSAs data in ROI2 that contains 49 pixels, totaling in 147 measurements over the same 12-s time range.
329 The standard DEM inversion techniques assume the so-called coronal elemental abundances, where the
330 Fe abundance is four times larger than in the photosphere. It was reported^{28,29}, however, that in flaring
331 volumes the abundance can be closer to the photospheric one due to the fact that the thermal plasma
332 is mainly due to chromospheric evaporation of material with photospheric abundance initiated by the
333 precipitation of flare-accelerated particles into the chromospheric footpoint. Therefore, we employed
334 the AIA thermal plasma diagnostics assuming alternately both the coronal and photospheric abundance.
335 Another possible source of uncertainty of the EUV diagnostics is an assumption of ionization equilibrium,
336 which can be strongly violated during nonequilibrium flaring conditions. In addition, the EUV diagnostics
337 suffer more from potential contributions along a long LOS (due to the dependence of EM on the column
338 depth), compared with the microwave diagnostics, which are restricted to the region inside the nonthermal
339 gyrosynchrotron source only.

340 With all these reservations in mind, Fig. S5b shows a histogram of the thermal number density from
341 the described rectangular ROI assuming the coronal abundance in filled dark blue and the photospheric
342 abundance in empty dark blue. The filled light blue histogram shows the distribution of the thermal
343 electron number density obtained for the three time frames for the entirety of ROI2. These distributions
344 agree with each other within a factor of two (less for the photospheric abundance case), confirming that
345 the thermal electron number densities derived from the microwave diagnostics in ROI2, where they are
346 statistically well constrained, are consistent with the EUV derived numbers. We cannot perform a similar
347 exercise in ROI1 because the microwave diagnostics of n_{th} does not offer well-constrained values.

348 **Supplementary Videos**

349 **Supplementary Video S1. Evolving maps of the coronal parameters of the solar flare.** This Supple-
350 mentary Video demonstrates evolution of the thermal number density, nonthermal number density, and
351 spectral index δ of the suprathermal electron distribution over energy in the 2017 September 10 flare over
352 the four minutes. Each frame is separated by 4 seconds. Solid white contour outlines ROI1.

353 **Supplementary Video S2. Acceleration efficiency vs electron spectral index δ .** This Supplementary
354 Video demonstrates how the proxy of the acceleration efficiency, r_B (panel a), and the spectral index δ
355 (panel b) evolve, and how they establish a correlation as time progresses (panel c). The video layout is the
356 same as of Fig. 3.

357 **Supplementary Video S3. Sensitivity of total intensity of the microwave emission to variation of
358 source parameters.** This movie demonstrates how the total intensity (Stokes I) of the microwave emission
359 varies when the parameters of the emission source change one by one. Note, in particular, the effect of n_{th}
360 and E_{min} .

361 **Code availability**

362 All the codes we use in this study are based on publicly available software packages: GSFIT is available
363 in the community-contributed SolarSoftWare repository, under the packages category, at www.lmsal.org.

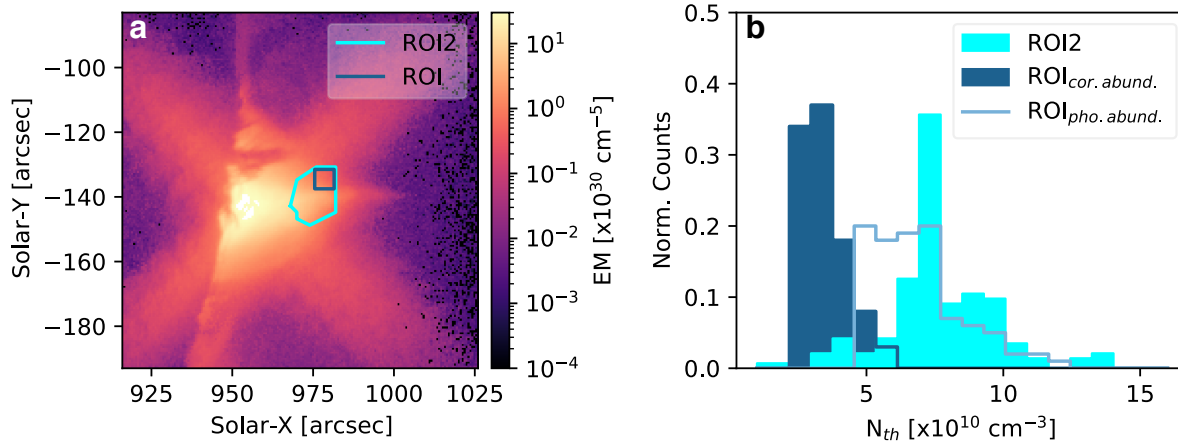


Fig. S5. Comparison of thermal plasma density diagnostics. a: Emission Measure (EM) map obtained at 15:58 UT over the temperature range of 0.5–30 MK. b: Histogram of the distribution of the thermal electron number density n_{th} in the ROI2 and ROI obtained from microwave and EUV diagnostics, respectively.

364 com/solarsoft/ssw/packages/gsfitt/; the open-source MCMC code is documented in²⁶.

365 Data availability:

366 All original EOVSAs are maintained in the EOVSAs website at <http://www.ovsa.njit.edu>.
 367 Original EOVSAs data used for this study are available at <http://www.ovsa.njit.edu/fits/IDB/20170910/IDB20170910155625/>. Fully processed EOVSAs spectral imaging data in IDL
 368 save format can be downloaded from http://ovsa.njit.edu/publications/fleishman_ea_science_2019/data/.
 369
 370

371 References

- 372 **25.** Nita, G. M., Hickish, J., MacMahon, D. & Gary, D. E. EOVSAs Implementation of a Spectral Kurtosis
 373 Correlator for Transient Detection and Classification. *Journal of Astronomical Instrumentation* **5**,
 374 1641009–7366 (2016).
 375 **26.** Foreman-Mackey, D. *et al.* emcee: The MCMC Hammer. *PASP* **125**, 306 (2013).
 376 **27.** Hannah, I. G. & Kontar, E. P. Differential emission measures from the regularized inversion of
 377 Hinode and SDO data. *Astronomy and Astrophysics* **539**, A146 (2012).
 378 **28.** Warren, H. P. Measurements of Absolute Abundances in Solar Flares. *ApJ* **786**, L2 (2014).
 379 **29.** Doschek, G. A. *et al.* Photospheric and Coronal Abundances in an X8.3 Class Limb Flare. *Astrophys.*
 380 *J.* **853**, 178 (2018).

381 Corresponding author

382 Correspondence to [Gregory Fleishman](mailto:gfleishm@njit.edu) gfleishm@njit.edu.

383 **Acknowledgments:**

384 We thank the scientists and engineers who helped design and build EOVSAs, especially Gordon Hurford,
385 Stephen White, James McTiernan, Wes Grammer, and Kjell Nelin. This work was supported in part by
386 NSF grants AGS-2121632, AGS-1817277, AGS-1817277, AST-1910354, AGS-2130832, AGS-1654382,
387 and NASA grants 80NSSC18K0667, 80NSSC20K1318, 80NSSC19K0068, and 80NSSC18K1128 to New
388 Jersey Institute of Technology.

389 **Author contributions:**

390 G . D . F developed the model spectral fitting methodology, participated in model fitting and analysis of
391 the results, and wrote the draft manuscript; G . M . N developed the `GSFIT` spectral fitting package, and
392 participated in model fitting and analysis of results. B . C developed the microwave spectral imaging and
393 self-calibration strategy and adopted the MCMC methodology to perform the testing of the model fitting
394 validity; S . Y implemented the code of the microwave imaging pipeline under the guidance of D . E . G and
395 B . C and performed the consistency check between the microwave and EUV diagnostics. D . E . G led the
396 construction and commissioning of the EOVSAs and developed the observational strategy and calibration
397 for microwave spectroscopy. All authors discussed the interpretation of the data, contributed scientific
398 results, and helped prepare the paper.

399 **Competing interests:**

400 The authors declare that they have no competing financial interests.